This is the peer reviewed version of the following article Green Chem., 2017,19, 2361-2370 which has been published in final form

http://pubs.rsc.org/en/content/articlelanding/2017/gc/c6gc02586b#!divAbstract

Interfacial acidity in ligand-modified ruthenium nanoparticles boosts the performance for the continuous hydrogenation of levulinic acid to gamma-valerolactone

Davide Albani,[†,a] Qiang Li,[†,b] Gianvito Vilé,[a] Sharon Mitchell,[a] Neyvis Almora-Barrios,[b] Peter T. Witte,[c] Núria López,*[b] and Javier Pérez-Ramírez*[a]

Gamma-valerolactone (GVL), a versatile renewable compound listed among the top 10 most promising platform chemical by the US Department of Energy, is produced *via* hydrogenation of levulinic acid (LA). The traditional high-loading ruthenium-on-carbon catalyst (5 wt.% Ru) employed for this transformation suffers from low metal utilisation and poor resistance to deactivation due to the formation of RuO_x species. Aiming at an improved catalyst design, we have prepared ruthenium nanoparticles modified with the water-soluble hydroxyethyl-dimethyl ammonium dihydrogen phosphate (HHDMA) ligand and supported on $TiSi_2O_6$. The hybrid catalyst has been characterised by ICP-OES, elemental analysis, TGA, DRIFTS, H_2-TPR, STEM, EDX, ^{31}P and ^{13}C MAS-NMR, and XPS. When evaluated in the continuous-flow hydrogenation of LA, the Ru-HHDMA/$TiSi_2O_6$ catalyst (0.24 wt.% Ru) displays a fourfold higher reaction rate than the state-of-the-art Ru/C catalyst, while maintaining a 100% selectivity to GVL and no sign of deactivation after 15 hours on stream. An in-depth molecular analysis by Density Functional Theory demonstrates that the intrinsic acidic properties of the ligand-metal interface under reaction conditions ensure that the less energy demanding path is followed. The reaction does not obey the expected cascade mechanism and intercalates hydrogenation steps, hydroxyl/water eliminations, and ring closings to ensure high selectivity. Moreover, the interfacial acidity increases the robustness of the material against ruthenium oxide formation. These results provide valuable improvements for the sustainable production of GLV and insights for the rationalisation of the exceptional selectivity of Ru-based catalysts.

Introduction

The necessity for more sustainable products and processes has led to the use of new methodologies which result in a low carbon footprint. This implies, in line with the 12 principles of green chemistry,[1,2] the utilisation of biomass-derived reactive substrates, non-toxic solvents (*e.g.*, water), sustainable heterogeneous catalysts based on low precious metal loadings, and continuous-flow processes.[3] Gamma-valerolactone (GVL), for example, has been recognised by the US Department of Energy as an important bio-derived platform chemical.[4-8] This compound can be used for the manufacture of a number of important commodities such as transportation fuels, polymer intermediates, pharmaceuticals, food ingredients, or it can be directly applied as a renewable organic solvent. Gamma-valerolactone is synthesised from levulinic acid *via* a two-step process involving a selective hydrogenation and an intramolecular dehydration.[8,9] Ruthenium-based catalysts are widely applied for this reaction,[10] due to the intrinsic ability of this metal to selectively hydrogenate the C=O bond without reducing other unsaturated functionalities.[11] Nonetheless, conventional catalysts, such as 5 wt.% Ru/C, have some drawbacks, including the high metal content, possible metal leaching in water-based solvents, and oxidation to RuO_2 that can lead to severe activity losses.[12,13] In order to increase stability, some authors have proposed the utilisation of RuRe, RuSn, and RuPd alloys.[14-16] Similarly, it has been postulated that acidic moieties surrounding the catalytically active surface could be beneficial to reduce the extent of deactivation.[17-20]

Alternative active phases to Ru, such as Cu,[21] Pt,[22] Ni,[23] , Pd,[24] Ir,[24] and Au[25], are much less selective, yielding 2-methyltetrahydrofuran and 1,4-pentandiol, and/or require harsher reaction condition to reach the same conversion level. Applications of nanostructured hybrid materials in catalysis are continuously expanding due to the unique properties that can arise from the interaction of the organic and inorganic components.[26-28] In fact, their chemical versatility makes these materials attractive for the possibility to combine the advantages of heterogeneous catalysts (*e.g.*, easy separation of the catalyst from the reaction mixture) with the intrinsic selectivity encountered over homogeneous catalysts.[29] In the last years, a key development in the application of hybrid materials for selective hydrogenations was the identification of hydroxyethyl-dimethyl ammonium dihydrogen phosphate (HHDMA) as a suitable ligand for the synthesis of metal nanoparticles.[30,31] This molecule integrates both stabilising and reducing properties and can be applied in aqueous medium, eliminating many hurdles which have long hampered the industrial exploitation of other routes to prepare hybrid nanoparticles (*e.g.*, the need to use

low-boiling point solvents, the fast addition of expensive or toxic reductants). This enabled the production of hybrid Pd-HHDMA and Pt-HHDMA catalysts for alkyne and nitro-group hydrogenation, respectively, commercialised by BASF under the trademark NanoSelect.[32-35] Due to the presence of a dihydrogen phosphate head, the HHDMA ligand acts as a pH buffer, controlling the local acidity. This can be utilised for attaining beneficial effects in terms of reaction rate, while retaining high selectivity levels. Since the selective hydrogenation of levulinic acid requires catalyst acidity to improve the performance, we decided to prepare and catalytically explore for the first time HHDMA-modified Ru nanoparticles.

From a process viewpoint, the hydrogenation of levulinic acid to GVL have been traditionally conducted in batch reactors,[21-25,36] mainly due to the simplicity of the equipment. However, it is now widely recognised that continuous-flow reactors offer important benefits in terms of process intensification, safety, evaluation of deactivation phenomena, and kinetic analysis under steady state.[37] For these reasons, in recent times, several authors have explored the selective hydrogenation of levulinic acid in continuous mode.[13,25,38-41]

Herein, we report the synthesis of Ru-HHDMA colloids displaying a narrow particle size distribution centred at 1.5 nm, and the subsequent deposition onto a $TiSi_2O_6$ carrier. Characterisation by inductively coupled plasma optical emission spectroscopy, elemental analysis, scanning transmission electron microscopy, energy dispersive X-ray mapping, ^{31}P and ^{13}C magic angle spinning nuclear magnetic resonance, X-ray photoelectron spectroscopy, diffuse reflectance infrared spectroscopy, and temperature-programmed reduction with H_2 confirms the desired interaction of the ligand and the metal nanoparticle in the resulting catalyst. In order to explore the advantages of ligand modification in comparison with the state-of-the-art Ru/C material, the catalyst performance has been evaluated in the continuous-flow three-phase hydrogenation of levulinic acid to γ-valerolactone in water at different temperatures, pressures, and flow rates. Density Functional Theory has been employed to derive mechanistic understanding of the high selectivity to GVL achieved over Ru-based catalysts and the enhanced activity of the ligand-modified nanoparticles.

Experimental

Catalyst preparation. As depicted in **Figure 1**, an aqueous solution of HHDMA (7 cm^3, 30%) was diluted in deionised water (200 cm^3) and mixed with an aqueous solution of $RuCl_3$ (2 cm^3, 0.5 M) and HCl (0.5 cm^3, 33%). The resulting mixture, containing 0.5 mg Ru cm^{-3}, was heated to 368 K and stirred at this temperature for 2 h to form colloidal metal nanoparticles of approximately 1.5 nm. The colloidal solution was added to a suspension consisting of $TiSi_2O_6$ (Aldrich, 30 g) and deionised water (300 cm^3). The suspension was stirred for 1 h, filtered extensively with deionised water, and dried overnight at 333 K. The Ru/C catalyst (Sigma-Aldrich, ref.: 24888169) was commercially available. Prior to use, this material was reduced at 473 K for 1 h flowing 10 vol.% H_2/N_2 (20 cm^3 min^{-1}) using a heating rate of 10 K min^{-1}.

Catalyst characterisation. The ruthenium content in the catalysts was determined by inductively coupled plasma-optical emission spectrometry (ICP-OES) using a Horiba Ultra 2 instrument equipped with photomultiplier tube detection. The C, H, N, and P contents were determined by infrared spectroscopy using a LECO CHN-900 combustion furnace. Nitrogen isotherms were measured at 77 K in a Micrometrics ASAP 2020, after evacuation of the samples at 393 K for 3 h. High-angle annular dark field scanning transmission electron microscopy (HAADF-STEM) images and elemental maps by energy dispersive X-ray (EDX) spectroscopy were acquired using an FEI Talos S200 microscope operated at 200 kV, with 70 mm C2 aperture and 0.4 nA beam current. The catalysts were dispersed as dry powders on lacey carbon coated copper grids. The particle size distribution was assessed by counting more than 150 individual Ru nanoparticles. H_2 chemisorption was performed using a Thermo TPDRO 1100 unit. The samples were treated in He (20 cm^3 min^{-1}) at 393 K for 60 min and reduced in 5 vol.% H_2/N_2 (20 cm^3 min^{-1}) at 423 K for 30 min. Then, pulses of 5 vol.% H_2/N_2 (0.344 cm^3) were dosed to the catalyst at 308 K every 4 min. The ruthenium

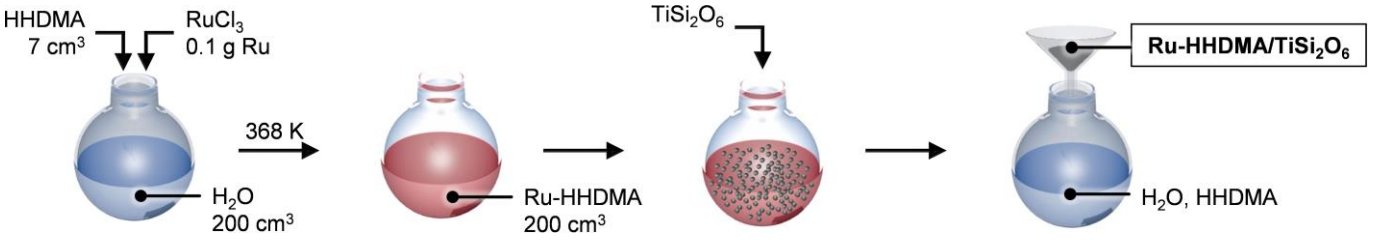

Fig. 1 Synthetic steps involved in the preparation of the Ru-HHDMA/$TiSi_2O_6$ catalyst.

Table 1. Characterisation data of the catalysts.

Catalyst	Ru[a] / wt.%	C[a] / wt.%	H[a] / wt.%	N[a] / wt.%	P[a] / wt.%	Weight loss[b] / %	S_{BET}[c] / $m^2\ g^{-1}$	V_{pore}[d] / $cm^3\ g^{-1}$	d_{Ru}[e] / nm
Ru-HHDMA/$TiSi_2O_6$	0.24	4.5	1.8	0.3	0.9	12	281	0.21	1.3
Ru/C	5.0	95	-	-	-	-	755	0.65	1.5

[a]Inductively coupled plasma optical emission spectroscopy; [b]Elemental analysis; [c]Thermogravimetric analysis; [d]BET method; [e]V_{ads} *at* p/p_0 = 0.95; [f]Scanning transmission electron microscopy.

dispersion was calculated from the amount of chemisorbed H_2, considering an atomic surface density of 1.57×10^{19} atoms m^{-2} and an adsorption stoichiometry $Ru/H_2 = 2$.[42] Temperature-programmed reduction with hydrogen (H_2-TPR) was performed using a Micromeritics Autochem II 2920 unit connected to a MKS Cirrus 2 quadrupole mass spectrometer. The samples (0.1 g) were treated in He flow (20 $cm^3\ min^{-1}$) at 393 K for 1 h, cooled down to 308 K, and finally heated to 1273 K (10 K min^{-1}) while monitoring the consumption of H_2. X-ray photoelectron spectroscopy (XPS) was conducted in a Physical Electronics Instruments Quantum 2000 spectrometer using monochromatic Al Kα radiation generated from an electron beam operated at 15 kV and 32.3 W. The spectra were collected under ultra-high vacuum conditions (residual pressure = 5×10^{-8} Pa) at a pass energy of 50 eV. In order to compensate for charging effects, all binding energies were referenced to the C 1*s* at 288.2 eV. Thermogravimetric analysis was performed in a Mettler Toledo TGA/DSC 1 Star system. Prior to measurement, the samples were dried in N_2 (40 $cm^3\ min^{-1}$) at 393 K for 1 h. The analysis was performed in air (40 $cm^3\ min^{-1}$), heating the sample from 298 K to 1173 K at a rate of 10 K min^{-1}. ^{13}C and ^{31}P magic-angle spinning nuclear magnetic resonance (MAS NMR) spectra were recorded on a Bruker AVANCE III HD NMR spectrometer at a magnetic field of 16.4 T corresponding to a ^1H Larmor frequency of 700.13 MHz. A 4 mm double resonance probe head at a spinning speed of 10 kHz was used for all experiments. The ^{13}C spectra were acquired using cross polarization mode with a contact time of 2.00 ms and a recycle delay of 1 s. A total of 64×10^3 scans were added for each sample. The ^{31}P experiments used a single pulse excitation sequence with a recycle delay of 1 s. Between 39×10^3 and 96×10^3 scans were acquired depending on the sample. Both ^{13}C and ^{31}P experiments used high-power ^1H decoupling during acquisition with SPINAL-64 sequence. Fourier transform infrared (FTIR) spectroscopy was performed in a Bruker Optics Vertex 70 spectrometer equipped with high temperature cell, ZnSe windows, and a mercury-cadmium-telluride (MCT) detector. The cell was filled with powdered catalyst diluted with KBr in a weight ratio (1:10) and carefully levelled to minimise reflection from the sample surface. The spectra were recorded in He (20 $cm^3\ min^{-1}$) at 473 K, accumulating 64 scans in the 4000-1000 cm^{-1} range with a resolution of 4 cm^{-1}.

Catalyst testing. The hydrogenation of levulinic acid (ABCR, 98%) was carried out in a fully-automated flooded-bed reactor (ThalesNano H-Cube Pro™), in which the gaseous hydrogen produced *in situ via* electrolysis of Millipore water and the liquid feed (containing 5 wt.% of substrate and deionised water as solvent) flow concurrently upward through a cylindrical cartridge of approximately 3.5 mm internal diameter. The latter contained a fixed bed composed of the catalyst (0.1 g of Ru-HHDMA/$TiSi_2O_6$ or 0.05 g of Ru/C) well mixed with inert titanium silicate as diluent (0.12 g, Sigma-Aldrich, 99.8%), both with particle size of 0.2-0.4 mm. The reactions were conducted at various temperatures (373-423 K), total pressures (1-60 bar), and liquid flow rate (0.3-1.2 $cm^3\ min^{-1}$, resulting in contact times (τ) between 4-16 s), keeping constant the H_2 flow rate (56 $cm^3\ min^{-1}$). For every experimental condition, three data points were averaged. In particular, the products were collected after 20 min at each experimental condition; this was appropriate, considering that, in our continuous-flow microreactor, steady-state operation is reached in 5-10 min. The product composition was analysed offline by high-performance liquid chromatography (HPLC), using a Merck LaChrome system equipped with a HPX-87H column, refraction index and UV-Vis detectors. A 0.005 M aqueous H_2SO_4 solution flowing at 0.600 $cm^3\ min^{-1}$ was used as eluent. The conversion (*X*) of a given substrate was determined as the amount of reacted levulinic acid divided by the amount of substrate at the reactor inlet. The reaction rate (*r*) was expressed as the number of moles of LA reacted per hour and mole of Ru in the catalyst. The selectivity (*S*) to each product was quantified as the amount of the particular product divided by the amount of reacted levulinic acid.

Computational details. Density Functional Theory (DFT) calculations were performed using the Vienna *ab-initio* Simulation Package (VASP),[43,44] employing the generalised gradient approximation with the revised Perdew-Burke-Ernzerhof exchange-correlation functional.[45] Since van der Waals (vdW) contributions are required to effectively model large molecules such as LA and HHDMA, the Grimme DFT-D2 method[46,47] modified with C6 parameters developed in our group has been applied.[48] The interaction between valence and core electrons was described by the projector augmented wave (PAW) pseudopotencials[49,50] with cut-off energy of 450 eV. The calculated lattice parameters for Ru (2.712 Å with c/a = 1.582) agrees well with the experimental one (2.706 Å with c/a = 1.584).[51] Gas-phase molecules such as LA and GVL were optimised in a simulation box of 20×20×20 $Å^3$. The Ru/C catalyst (Ru(0001)) was modelled using periodic slabs with a thickness of five layer and in a p(4×4) supercell, while for the Ru-HHDMA four dihydrogenophophates and the cationic head of the surfactant were included.[33] The slabs were separated from the neighbouring ones through a vacuum gap of 20 Å to avoid lateral interactions. In particular, the two upmost layers were completely relaxed, whereas the atoms in the remaining layers were fixed to mimic the bulk**.** The calculation of the adsorption and transition state energies was performed with a 3×3×1 *k*-point. Dipole corrections were introduced to eliminate the spurious contributions arising from the asymmetry of the system. Solvation contributions for the

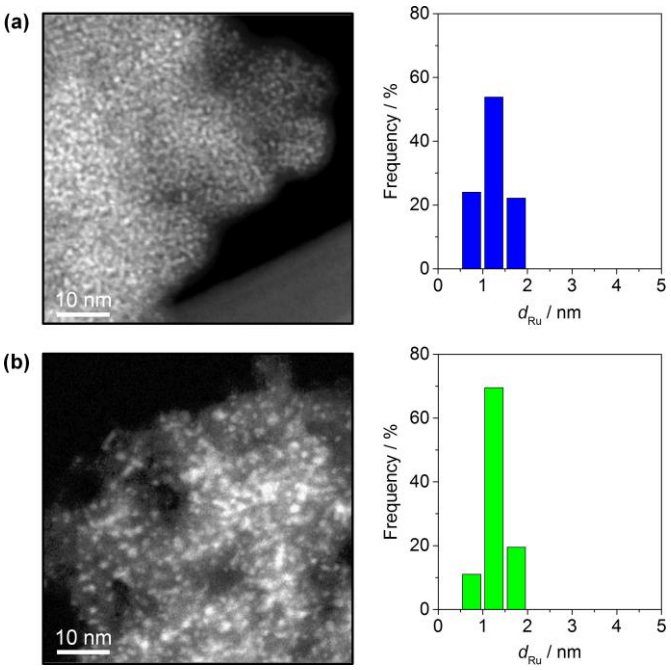

Fig. 2 Scanning transmission electron micrographs and particle size distributions of Ru-HHDMA/$TiSi_2O_6$ (a) and Ru/C (b).

molecules in the liquid phase were also considered using the MGCM methodology.[52] The climbing image nudged elastic band (CI-NEB)[53,54] and improved dimer method (IDM)[55] were employed to locate the transition states in the potential surfaces. The transition states were confirmed by having only one imaginary value from frequency analysis.

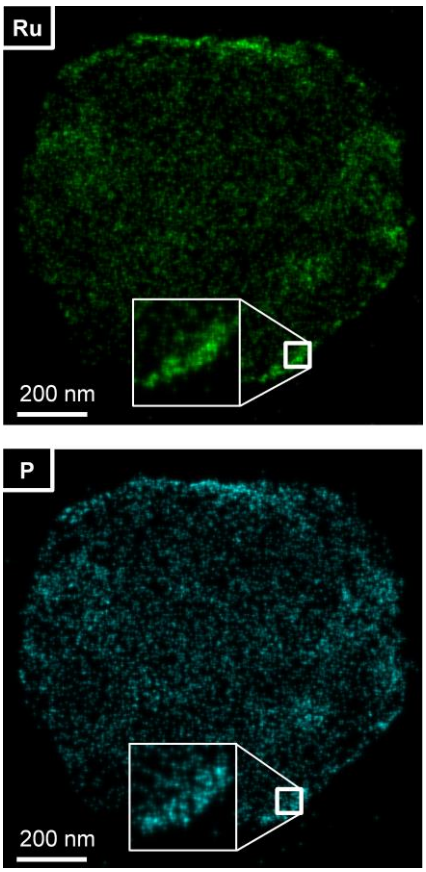

Fig. 3 Energy dispersive X-ray maps of Ru and P in Ru-HHDMA/$TiSi_2O_6$. The insets show a zoom of 2 times.

Results and Discussion

Catalysts properties. Table 1 shows the bulk composition and morphological characteristics of the materials prepared. ICP-OES analysis of the Ru/C and Ru-HHDMA/$TiSi_2O_6$ catalysts reveal a total ruthenium content of 5 and 0.24 wt.%, respectively. In particular, for the latter material, the presence of ligand is confirmed by C, H, N, and P analysis. Considering the stoichiometry of the surfactant ($C_{20}H_{46}NO_5P$), it is possible to estimate a total ligand concentration of *ca*. 10 wt.%. Inspection of the scanning transmission electron micrographs reveals that the ruthenium nanoparticles possess a uniform spherical shape, with an average particle diameter of around 1.5 nm in both cases (Figure 2). As reported by Philippot *et al.*,[56] this is unsurprising since small Ru particles readily form due to the strong intrinsic interaction of this metal with a variety of C, Ti, and Si-based supports. The nanoparticles are well distributed and no evidence of particle agglomeration is observed. Characterisation by N_2 sorption confirms the distinct textural properties of the two catalysts (Figure S1). In particular, the Ru-HHDMA catalyst exhibits the typical total surface area (200 $m^2\ g^{-1}$) of titanium silicate carriers, and a high (meso)porosity. The corresponding pore size distribution derived by the Barrett-Joyner-Halenda model evidences a discrete range of pore sizes centred around 10 nm. In contrast, the Ru/C catalyst displays the surface area is 755 $m^2\ g^{-1}$, owing to the high microporosity evidenced by the high uptake in the N_2 adsorption isotherm at low relative pressures. To confirm the microporous nature of the carbon support, an NLDFT model assuming slit-pore geometry has been employed, which evidenced a pore size distribution centred at 0.8 nm. In order to characterise the ligand distribution over the catalyst, EDX mapping was performed over Ru-HHDMA/$TiSi_2O_6$ (Figure 3). Interestingly, phosphorous appears to be mainly localised in the areas where Ru is also present, corroborating previous hypotheses that the ligand is bound to the metallic nanoparticle through phosphate heads and to the carrier through N-OH dispersion interactions.[31] This clear partition between the type of ligand adsorbed on the nanoparticles and that on the support enable, for the first time, the direct estimation of the ligand content per nanoparticle. Assuming an hcp unit cell with atomic packing of 0.76,[57] and considering the dispersion of Ru, we have first calculated the moles of surface Ru atoms. The ratio between the moles of P obtained by elemental analysis and those of surface Ru provided the number of HHDMA molecule per nanoparticle (*ca*. 250 HHDMA molecules/nanoparticle). To determine the thermal stability of the ligand shell, thermogravimetric analysis in air was conducted (Figure 4a). In line with previous results,[33-35] the ligand decomposition started at 500-550 K, confirming that the metal-ligand interaction is independent from the metal identity. To further elucidate the chemical identity of the ligand molecule, DRIFT spectra were acquired on both the Ru-HHDMA/$TiSi_2O_6$ catalyst and the $TiSi_2O_6$ support (Figure 4b). The spectrum of the catalyst shows, between 3000-2800 cm^{-1}, the C-H vibrational mode of the aliphatic chain of the ligand and, between 1200-1100 cm^{-1}, the stretching mode of the phosphate group. In addition, the

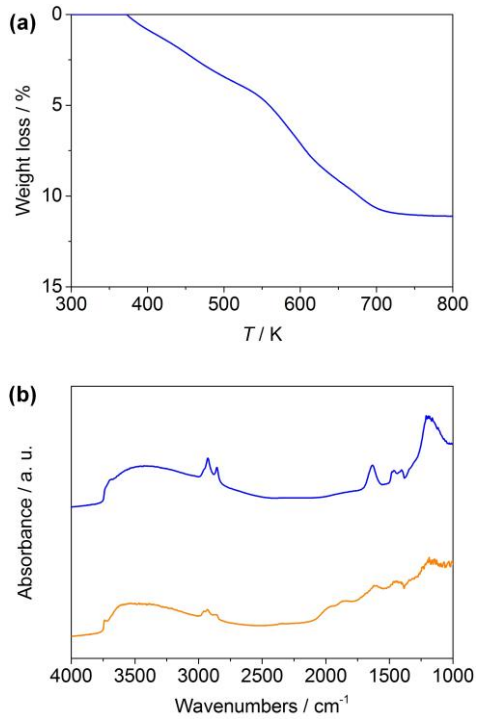

Fig. 4 Thermogravimetry of Ru-HHDMA/$TiSi_2O_6$ in air (a). DRIFT spectra of the Ru-HHDMA/$TiSi_2O_6$ catalyst (blue) and the $TiSi_2O_6$ carrier (orange).

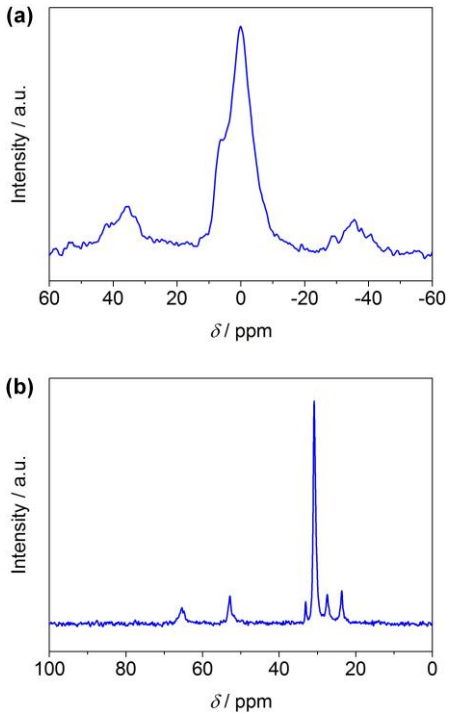

Fig. 5 ^{31}P (a) and ^{13}C (b) magic-angle spinning nuclear magnetic resonance spectroscopy of Ru-HHDMA/$TiSi_2O_6$.

broad band at 3500 cm^{-1}, which is present in both the support and catalysts, is attributed to stretching of O-H groups associated with the surface of the $TiSi_2O_6$ support.

The sample was further characterised by solid-state ^{13}C and ^{31}P MAS NMR. The ^{31}P MAS NMR spectra (Figure 5a) display a single, broad isotropic signal around 0 ppm, which is consistent with the presence of an orthophosphate anion. This peak is flanked on either side by a spinning sideband giving a rough estimate of the chemical shift anisotropy of about 50 ppm. Contrarily, the peaks in the ^{13}C MAS NMR spectra (Figure 5b) can be assigned in analogy with the signals observed in the solution state NMR spectra. The signals above 40 ppm all originate from carbon positions in close proximity to the nitrogen. These resonances display a markedly increased linewidth when compared to many of the peaks below 40 ppm, which mainly correspond to positions in the aliphatic tail of the molecule. These observations are consistent with previous findings,[35] indicating a reduced mobility (on the NMR timescale) of the head-group with respect to the tail, for which the signals are dynamically equilibrated. In fact, the ^{31}P peak with a full width at the half height of approximately 2 kHz seems to be inhomogeneous in nature and is indicative of a statically disordered environment.

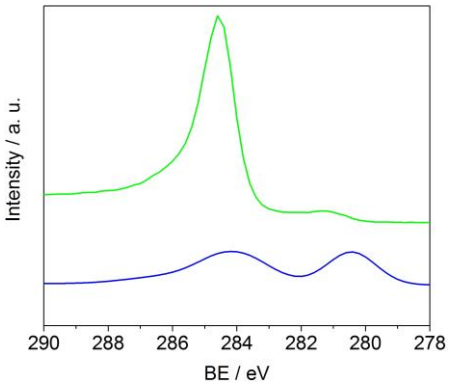

Fig. 6 Ru 3*d* core level X-ray photoelectron spectroscopy spectra of the Ru-HHDMA/$TiSi_2O_6$ (blue) and Ru/C (green).

Notwithstanding the determination of the atomic state of Ru-based materials is not straightforward for carbon supported material, due to the overlapping of the Ru 3d core level signal with C 1s one, a feature centred at 281.3 eV indicative of the presence of RuO_x species for the Ru/C sample was observed.[58] In the case of the Ru-HHDMA/$TiSi_2O_6$, a single Ru $3d_{5/2}$ core level at 280.2 eV was displayed (Figure 6), confirming that the ruthenium surface is fully metallic.[58,59] An additional tool to further prove the oxidation state of the Ru catalysts is H_2-TPR (Figure S2). Apart from the decreased signal intensity observed at room temperature due to the stabilisation of the MS filament, Ru-HHDMA/$TiSi_2O_6$ did not show any hydrogen consumption peak around 400 K, the expected temperature of reduction of RuO_x species to Ru^0.[60] In contrast, the Ru/C sample shows two peaks at 400 and 560 K. The first is attributed to the reduction of oxidic Ru species to metallic Ru, whereas the second represents the H_2 consumption due to the formation of methane catalysed by Ru.

Hydrogenation of levulinic acid. The performance of the Ru-based catalysts has been assessed in the continuous hydrogenation of levulinic acid in water (Figure 7, and 8). The contour maps in Figure 7 show the effect of temperature and pressure on levulinic acid conversion and on the selectivity to γ-valerolactone for Ru-HHDMA/$TiSi_2O_6$ and Ru/C. An excellent selectivity degree (>95%) was obtained at all temperatures and pressures investigated for both catalysts, highlighting the intrinsic selectivity of Ru-based materials for these types of chemical transformation (*vide infra*).

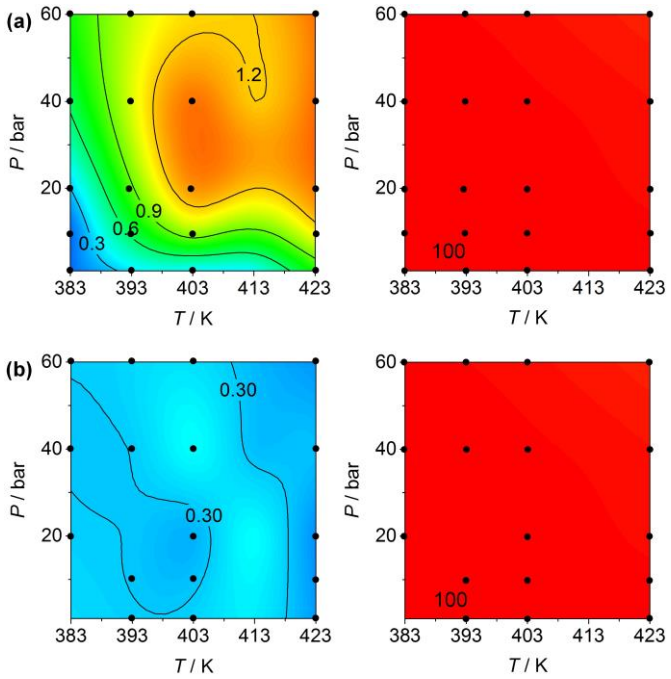

Fig. 7 Reaction rate (in 10^3 h^{-1}, left) and selectivity to γ-valerolactone (in %, right) as a function of temperature and pressure in the hydrogenation of levulinic acid over Ru-HHDMA/$TiSi_2O_6$ (a) and Ru/C (b). Conditions: F_L(levulinic acid+water) = 0.3 cm^3 min^{-1}, and $F_G(H_2)$ = 54 cm^3 min^{-1}. The contour maps were obtained through spline interpolation of the 20 experimental points indicated by black dots.

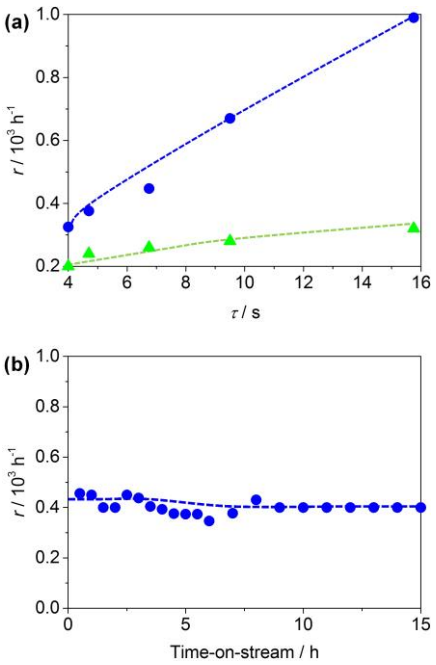

Fig. 8 Reaction rate (in 10^3 h^{-1}) as a function of the contact time (τ) in the hydrogenation of levulinic acid over Ru-HHDMA/$TiSi_2O_6$ (blue) and Ru/C (green) (a). Stability of Ru-HHDMA/$TiSi_2O_6$ in the hydrogenation of levulinic acid (b). Conditions: T = 403 K, P = 10 bar, F_L(levulinic acid+water) = 0.3-1.2 cm^3 min^{-1}, and $F_G(H_2)$ = 54 cm^3 min^{-1} (a); T = 393 K, P = 20 bar, F_L(levulinic acid+water) = 0.3 cm^3 min^{-1}, and $F_G(H_2)$ = 54 cm^3 min^{-1} (b).

1,4-pentanediol was also formed in the reaction, but with a selectivity lower than 5%. In term of reaction rate, the ligand-modified catalyst exhibits, at 403 K and 20 bar, a fourfold higher activity compared to the state-of-the-art catalyst, indicating that the combination of inorganic and organic counterparts boosts the catalytic activity (this important aspect is elaborated below). We have also studied the effect of the contact time (τ) on the reaction rate (r) for both catalysts. A linear increase of r with the contact time is observed in both cases (Figure 8a). Note that, even with four times longer residence times, high selectivity levels were retained, proving the intrinsic selectivity of Ru-based catalysts. In order to verify the stability against leaching of the hybrid catalyst, a long-term test was conducted. The catalyst was stable for 15 h on stream, displaying no signs of deactivation (Figure 8b). To further prove that both the ligand and the metal were retained after the reaction, elemental analysis of the used catalyst was conducted, showing negligible differences in loading of both Ru and ligand with respect to the fresh catalyst. Additionally, STEM micrographs of the used catalysts have been acquired to verify if the ligand can hinder the sintering of the Ru nanoparticles. Interestingly, as depicted in Figure S3, the average particle size was retained upon hydrogenation. Contrarily, as reported elsewhere,[61] extensive particle sintering is typically observed on Ru/C, confirming that the Ru nanoparticles are susceptible of clustering if not effectively shielded in the presence of water.

Mechanism over bare Ru nanoparticles. To obtain molecular insights on the mechanism of reaction over Ru and Ru-HHDMA surfaces, DFT calculations were conducted. Figure 9 depicts the generally accepted cascade mechanism for the conversion of LA to GVL.[6,62] LA would either undergo hydrogenation to produce 4-oxopentanal and 4-hydroxyentanoic acid, or intramolecular esterification to produce angelicalactone. It is important to highlight that this pathway only provides a macroscopic framework for the reaction. When considering the reaction from the microscopic viewpoint, the mechanism for LA and levulinate to GVL consists of numerous and much more complex elementary steps, including C-O bond cleavage, hydrogenation (protonation) of the oxygen atoms, hydrogenation of carbon in the ketone group, and ring closing steps. To construct a solid theoretical model, we have considered all 34 intermediates generated from the 68 corresponding elementary steps (see ESI, Figure S4 and S5). The sequence of these reactions could affect the result, determining the most preferable pathway. Due to the complexity of the reaction network, all the aforementioned steps have been first computed for a bare Ru nanoparticle and then extended to the Ru-HHDMA case (*vide infra*). To maximise the relevance of the theoretical calculations, DFT calculations using dispersion interactions have been applied. Besides, to determine the nature of the interaction between LA and the surface, we have also considered that the reactions take place in water, suggesting that LA, which is an acid with pK_a of 4.5, is prevalently in anionic state in aqueous solution. The first step of the reaction is hydrogen dissociation on the Ru metal surface, which is barrierless and exothermic (0.68 eV $atom^{-1}$). This step is followed by the adsorption of levulinate on the surface (black box in Figure 10 and ESI). As shown in Figure 10, once the levulinate is in the adsorbed state, several paths can follow: C-O cleavage, followed by ring closure, or hydrogenation. From the analysis of the reaction energies and energy barriers of all possible steps (see ESI), it emerges that mainly the hydrogenation of the ketonic group leading to 17-c is likely to occur. In fact this step needs a relatively

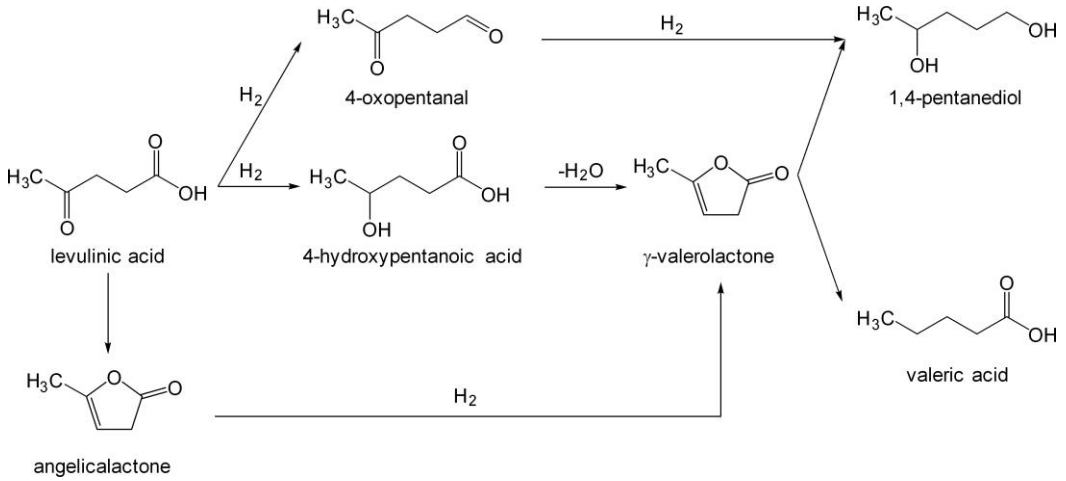

Figure 9. Cascade process for the hydrogenation of LA to GVL, 1,4-pentanediol, and valeric acid.

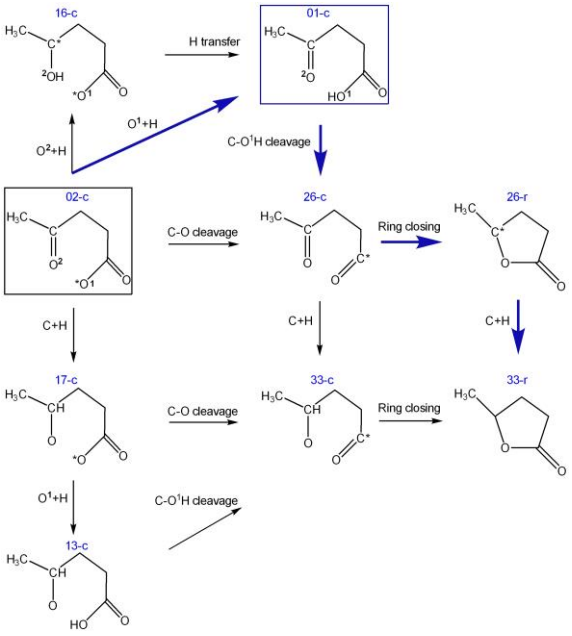

Figure 10. Reaction network for levulinic acid (blue)/levulinate to γ-valerolactone. Blue arrows describe the path for levulinic acid on Ru-HHDMA. Contrarily, all the steps are possible in the levulinate transformation on bare Ru nanoparticle.

low energy barrier (0.57 eV) compared to the competitive protonation of O^1 and O^2 (1.34 and 1.33 eV, respectively). Besides, the protonation of O^1 and O^2 are highly endothermic (0.69 and 1.13 eV). C-O cleavage of LA is also unlike to occur. In fact, the direct C-O bond scission from carboxylate group of levulinate (structure 02-c) and 17-c need large energy barriers (1.56 and 1.39 eV, respectively). These high barriers arise from the strong interaction of the metal surface with the bidentate O atoms from COO^- which is η^2-O,O coordinated to the surface. Since the reaction is carried out in water, we have investigated the possibility that the solvent assists the C-O cleavage,[63] resulting in a barrier decrease to 1.08 and 1.17 eV, respectively. Since these barriers remain pretty large, only moderate contributions from ring closing reactions are expected from R-COO^- species, due to the strong binding of the O of the carboxyl group, inhibiting the internal C-O bond formation. Thus, after the formation of 17-c, the water-assisted C-O cleavage takes place, leading to the formation of 33-c that gives the final product, GVL (33-r) *via* ring closing. The C-O bond breaking is the rate determining step of the whole process. Notice, however, that the reaction network can encompass other species, like those shown in Figure 9, and that a complete reaction rate analysis with the contribution of the different paths under different conditions would require a full microkinetic analysis including coverage effects.

The thermodynamic selectivity concept, which refers to the energy difference between the adsorption of the reactants and that of the products, is one the simplest descriptor that can be used to rationalise activity-selectivity patterns of challenging hydrogenation reactions.[64-66] High thermodynamic selectivity requires that the reactants are much more strongly adsorbed to the catalyst surface than the products. This concept can be applied here to rationalise the high product selectivity obtained in the reaction. Specifically, GVL over-hydrogenation cannot occur since the calculated barrier for this step is approximately 1.36 eV. This is higher that the desorption barrier for GVL (1.24 eV, which reduces to 0.36 eV considering the solvation phenomena). Thus, once GVL is formed, it easily desorbs from the surface.

Mechanism over Ru-HHDMA. Since the reaction network is very complex, the role of the Ru-HHDMA can be inferred from the Ru(0001) network, and complemented with a few calculations on the modelled Ru-HHDMA interface. The preferred path on Ru-HHDMA is highlighted by the blue arrows in Figure 10. The major molecular difference in the mechanism of reaction over the Ru-HHDMA surface is in the activation of molecular H_2. Due to the presence of HHDMA ligands, hydrogen dissociation is barrierless and exothermic on the Ru-HHDMA interface (0.45 eV $atom^{-1}$). This facilitated hydrogen activation produces a buffer of hydrogen atoms that at high coverage can be stabilised between the phosphate anions and co-adsorbed water. Particularly, part of these hydrogen atoms can be trapped in the form of hydronium (H_3O^+) species. These protons being more acidic than LA reverse the equilibrium of the reactant towards its acidic form (LA), instead of the anionic intermediate described above. This trapping is almost thermoneutral (+0.12 eV). Thus, when adsorbing the levulinate to the Ru-HHDMA, the proton buffered at the interface is transferred, converting the levulinate adsorbate into LA

Table 2. The main elementary steps in the mechanisms for LA hydrogenation to GVL on Ru(0001) and Ru-HHDMA surface.

	Ru(0001)	Ru-HHDMA
Step 1	Adsorption of levulinate	Adsorption of levulinate
Step 2	C^2 hydrogenation	Protonation of levulinate to LA
Step 3	C—O breaking* from R-COO	C—OH breaking from R-COOH
Step 4	Ring closing to GVL	Ring closing
Step 5	GVL Desorption	C^2 hydrogenation to GVL
		GVL Desorption

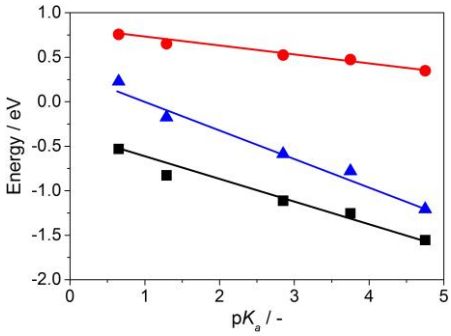

Figure 11. Relationship between pK_a and adsorption energy of the correspective carboxylate (E_{ads}, black), protonation energies (ΔE, red), as well as the sum of them ($E_{ads}+\Delta E$, blue). Liner fitting are: E_{ads} = (–0.23 ± 0.02)pK_a + (0.44 ± 0.06), ΔE = (–0.09 ± 0.01)pK_a + (0.80 ± 0.02), and $E_{ads}+\Delta E$ = (–0.32 ± 0.03)pK_a + (0.35 ± 0.08) with r^2 values of 0.97, 0.98, and 0.97, respectively. Estimated pK_a of the interface is 1.09.

(01-c, see the blue box in Figure 10). Due to the absence of hapticity (that is, the coordination of a ligand to a metal *via* a contiguous series of atoms), this does have a weaker interaction with the surface than $RCOO^-$ (02-c), and therefore the C-OH breaking from R-COOH (01-c to 26-c) features a lower barrier (0.46 eV) than any other reaction (*ca*. 1.0 eV). This enhanced C-OH cleavage results in the fourfold increase in the reaction rate observed experimentally (Table 2). After that, the ring closing takes place with a small barrier (0.44 eV), followed by the hydrogenation of 26-r to 33-r (0.87 eV).

To further characterise the intrinsic acidity of the surface, we have employed a set of small compounds: formic acid, acetic acid, chloro, dichloro, and trichloro acetic acid. In Figure 11, the adsorption energy of the corresponding anions (red) and the energy required to protonate them (black) have been calculated with respect to the anions in solution. The difference of those gives the adsorption energy of the acid (blue line). This energy equals to zero when the acid/anion are identical, enabling the determination of intrinsic pK_a of the Ru-HHDMA interface. From our calculations, the interface is buffered at pK_a = 1, indicating that reactions featuring molecules of lower pK_a would not benefit in terms of reaction rate. Similarly, Ru nanoparticles stabilised on reduced graphene oxide (GO) have also shown a fourfold increase in the activity when compared with standard Ru formulations.[12] Since in GO supports some acidic centres are retained even upon reduction, we believe that these centres can act as promoters in the same way as the interface does in Ru-HHDMA. This concept can be further transposed to any reaction catalysed by ionic liquids with sulfonate terminations.[67]

In order to rationalise the outstanding selectivity of Ru-based catalyst in breaking C-O bonds, a comparison with other metals could also be crucial. For instance, C-OH bond breaking on less oxophylic metals, such as Pd(111) and Pt(111) surfaces, presents high barriers (1.28 and 0.84 eV, respectively), while the competitive hydrogenations exhibit barriers of ca. 1 eV. Therefore, on these metals, the selectivity levels achieved are much lower since the activation energy window is very narrow.

Finally, considering that the main issue of Ru catalysts for biomass conversion is the relative instability against the formation of oxidic phases (RuO_x),[12] the ligand-modified catalyst was tested in a stability test (*vide supra*) and complemented with the analysis of oxygen adsorption. We have found that the adsorption of large quantities of oxygen on the Ru-HHDMA nanoparticles is inhibited due to the repulsion of the orthophosphate group (see ESI, Table S3 and Figure S6). Under H_2 atmosphere, the interface acidity modulates the oxidative effect of the oxygens as converts them into hydroxyls less prone to oxide formation. These computational results give the key for the outstanding selectivity of Ru-based catalyst in the conversion of LA to GVL, indicating that acid properties at the interface improve the activity and the stability of the Ru-HHDMA nanoparticles.

Conclusions

We have prepared and characterised a new type of hybrid Ru nanoparticles using HHDMA as a modifier. ICP-OES, elemental analysis, TGA, DRIFTS, H_2-TPR, STEM, EDX, ^{31}P and ^{13}C MAS-NMR, and XPS have been used for confirming the ligand-metal interaction and determining textural and spectroscopic features of the catalyst. The catalyst was evaluated in the continuous-flow hydrogenation of LA in water. At all conditions screened (T = 373-423 K, P = 1-60 bar, and τ = 4-16 s), Ru-HHDMA/$TiSi_2O_6$ displays an outstanding fourfold higher reaction rate than that of the benchmark 5 wt.% Ru/C catalyst, and full selectivity to GVL. Since the Ru/C catalyst is known to deactivate easily in water, a stability test over the ligand-modified has been carried out, showing no sign of deactivation for 15 h on stream. Density Functional Theory has unravelled the reasons behind this remarkable activity and intrinsic selectivity of Ru-HHDMA catalyst in the selective hydrogenation of levulinic acid. In particular, the metal/surfactant/water interface creates a local increase in the pH that can protonate the levulinate anion, resulting in a reaction network featuring low barriers and a fourfold reaction rate increase. Due to the structure of the nanocatalysts, this enhancement is maintained, demonstrating the robustness of the catalytic system. The high selectivity is of thermodynamic nature, meaning that once GVL is formed, it is easily desorbed from the surface, avoiding further hydrogenation. Contrary from the deactivation suffered by the Ru/C catalyst due to surface oxidation, the formation of RuO_x compounds in the ligand-modified catalyst is impeded for two reasons: the phosphate anions at the surface shield the nanoparticle, thus, reducing the oxygen uptake from by-products, and the high pH at the interface does not allow the formation of the oxide.

Acknowledgements

Financial support from ETH Zurich, ICIQ Foundation, and the Spanish Ministerio de Economía y Competitividad (CTQ2012-33826 and "Ayuda formación Posdoctoral" Fellowship (N.A-B.)) are acknowledged. Dr Roland Hauert (EMPA, Dubendorf) and Dr Réne Verel are acknowledged for the XPS analyses, and ^{13}C and ^{31}P MAS-NMR, respectively. ScopeM of the Swiss Federal Institute of Technology is acknowledged for providing access to its facilities. BSC-RES is thanked for generous computational resources.

References

1 P. Anastas and N. Eghbali, *Chem. Soc. Rev*., 2010, **39**, 301.
2 C. O. Tuck, E. Pérez, I. T. Horváth, R. A. Sheldon and M. Poliakoff, *Science*, 2012, **337**, 695.
3 R. A. Sheldon, *Green Chem.*, 2014, **16**, 950.
4 D. M. Alonso, S. G. Wettstein and J. A. Dumesic, *Green Chem*., 2013, **15**, 584.
5 I. T. Horváth, H. Mehdi, V. Fábos, L. Bode and L. T. Mika, *Green Chem*., 2008, **10**, 238.
6 M. Besson, P. Gallezot and C. Pinel, *Chem. Rev*., 2014, **114**, 1827.
7 R. Palkovits, *Angew. Chem. Int. Ed*., 2010, **49**, 4336.
8 F. D. Pileidis and M.-M. Titirici, *ChemSusChem*, 2016, **9**, 562.
9 A. Corma, S. Iborra and A. Velty, *Chem. Rev*., 2007, **107**, 2411.
10 W. R. H. Wright and R. Palkovits, *ChemSusChem,* 2012, **5**, 1657.
11 C. Michel and P. Gallezot, *ACS Catal*., 2015, **5**, 4130.
12 C. Xiao, T.-W. Goh, Z. Qi, S. Goes, K. Brashler, C. Perez and W. Huang, *ACS Catal.*, 2016, **6**, 593.
13 O. A. Abdelrahman, A. Heyden and J. Q. Bond, *ACS Catal.*, 2014, **4**, 1171.
14 S. G. Wettstein, J. Q. Bond, D. M. Alonso, H. N. Pham, A. K. Datye and J. A. Dumesic, *Appl. Catal., B*, 2012, **117**, 321.
15 D. J. Braden, C. A. Henao, J. Heltzel, C. C. Maravelias and J. A. Dumesic, *Green Chem*., 2011, **13**, 1755.
16 W. Luo, M. Sankar, A. M. Beale, Q. He, C. J. Kiely, P. C. A. Bruijnincx and B. M. Weckhuysen, *Nat. Comm*. 2016, 6:6540 doi: 10.1038/ncomms7540.
17 C. Moreno-Marrodan and P. Barbaro, *Green Chem*., 2014, **16**, 3434.
18 V. V. Kumar, G. Naresh, M. Sudhakar, C. Anjaneyulu, S. K. Bhargava, J. Tardio, V. K. Reddy, A. H. Padmasri and A. Venugopal, *RSC Adv*., 2016, **6**, 9872.
19 A. M. R. Galletti, C. Antonietti, V. De Luise and M. Martinelli, *Green Chem*., 2012, **14**, 688.
20 X. Zhang, P. Murria, Y. Jiang, W. Xiao, H. I. Kenttämaa, M. M. Abu-Omar and N. S. Mosier, *Green Chem*., 2016, **18**, 5219.
21 A. M. Hengne and C. V. Rode, *Green Chem*., 2012, **14**, 1064.
22 M. Sudhakar, V. V. Kumar, G. Naresh, M. L. Kantam, S. K. Bhargava and A. Venugopal, *Appl. Catal., B*, 2016, **180**, 113.
23 Z.-p. Yan, L. Lin and S. Liu, *Energy Fuels*, 2009, **23**, 3853.
24 L. E. Manzer, *Appl. Catal*., *A*, 2004, **272**, 249.
25 X.-L. Du, Q.-Y. Bi, Y.-M. Liu, Y. Cao and K.-N. Fan, *ChemSusChem*, 2011, **4**, 1838.
26 G. E. Oosterom, J. N. H. Reek, P. C. J. Kamer and P. W. N. M. van Leeuwen, *Angew. Chem. Int. Ed*., 2001, **40**, 1828.
27 V. I. Pârvulescu and C. Hardacre, *Chem. Rev*., 2007, **107**, 2615.
28 A. Kaushik, R. Kumar, S. K. Arya, M. Nair, B. D. Malhora and S. Bhansali, *Chem. Rev*., 2015, **115**, 4571.
29 M. A. Boles, D. Ling, T. Hyeon and D. V. Talapin, *Nat. Mater.*, 2016, **15**, 141.
30 P. T. Witte, P. H. Berben, S. Boland, E. H. Boymans, D. Vogt, J. W. Geus and J. G. Donkervoort, *Top. Catal*., 2012, **55**, 505.
31 P. T. Witte, S. Boland, F. Kirby, R. van Maanen, B. F. Bleeker, D. A. M. de Winter, J. A Post, J. W. Geus and P. H. Berben, *ChemCatChem*, 2013, **5**, 582.
32 E. H. Boymans, P. T. Witte and D. Vogt, *Catal. Sci. Technol*., 2015, **5**, 176.
33 G. Vilé, N. Almora-Barrios, S. Mitchell, N. López and J. Pérez-Ramírez, *Chem. Eur. J*., 2014, **20**, 5926.
34 G. Vilé, N. Almora-Barrios, N. López and J. Pérez-Ramírez, *ACS Catal*., 2015, **5**, 3767.
35 D. Albani, G. Vilé, S. Mitchell, P. T. Witte, N. Almora-Barrios, R. Verel, N. López and J. Pérez-Ramírez, *Catal. Sci. Technol*., 2016, **6**, 1621.
36 A. Yepez, S. De, M. S. Climent, A. A. Romero and R. Luque, *Appl. Sci.*, 2015, **5**, 532.
37 M. Irfan, T. N. Glasnov and C. O. Kappe, *ChemSusChem*, 2011, **4**, 300.
38 A. S. Piskun, J. E. de Haan, E. Wilbers, H. H. van de Bovenkamp, Z. Tang and H. J. Heeres, *ACS Suistainable Chem. Eng*., 2016, **4**, 2939.
39 R. A. Bourne, J. G. Stevens, J. Ke and M. Poliakoff, *Chem. Commun*., 2007, 4632.
40 J.-P. Lange, R. Price, P. M. Ayoub, J. Louis, L. Petrus, L. Clarke and H. Gosselink, *Angew. Chem. Int. Ed*., 2010, **49**, 4479.
41 J. M. Bermudez, J. A. Menéndez, A. A. Romero, E. Serrano, J. Garcia-Martinez and R. Luque, *Green Chem*., 2013, **15**, 2786.
42 J. Okal, M. Zawadzki, L. Kępiński, L. Krajczyk and W. Tylus, *Appl. Catal., A*, 2007, **319**, 202.
43 G. Kresse and J. Furthmüller, *Comput. Mater. Sci*., 1996, **6**, 15.
44 G. Kresse and J. Furthmüller, *Phys. Rev. B,* 1996, **54**, 11169.
45 J. P. Perdew, K. Burke and M. Ernzerhof, *Phys. Rev. Lett*., 1996, **77**, 3865.
46 S. Grimme, *J. Comput. Chem*., **2006**, 27, 1787.
47 T. Bučko, J. Hafner, S. Lebègue and J. G. Ángyán, *J. Phys. Chem. A*, 2010, **114**, 11814.
48 N. Almora-Barrios, G. Carchini, P. Błoński and N. López, *J. Chem. Theory Comput.*, 2014, **10**, 5002.
49 P. E. Blöchl, *Phys. Rev. B*, 1994, **50**, 17953.
50 G. Kresse and D. Joubert, *Phys. Rev. B*, 1999, **59**, 1758.
51 D. Lide, CRC Handbook of Chemistry and Physics, 84th Ed., CRC Press: Boca Ranton, 2003-2004.
52 M. Garcia-Ratés and N. López, *J. Chem. Theory Comput.,* 2016, **12**, 1331.
53 G. Henkelman and H. Jónsson, *J. Chem. Phys.*, 2000, **113**, 9978.

54 G. Henkelman, B. P. Uberuaga and H. Jónsson, *J. Chem. Phys.*, 2000, **113**, 9901.
55 A. Heyden, A. T. Bell and F. J. Keil, *J. Chem. Phys.,* 2005, **123**, 224101.
56 L. M. Martínez-Prieto, A. Ferry, L. Rakers, C. Richter, P. Lecante, K. Philippot, B. Chaudret and F. Glorius, *Chem. Commun*., 2016, **52**, 4768.
57 A. B. Ellis, M. J. Geselbracht, B. J. Johnson, G. C. Linsensky and W. R. Robinson, Teaching General Chemistry: A Material Science Companion, 1st Ed., American Chemical Society Publication, p. 103.
58 A. M. Ruppert, M. Jędrzejczyk, O. Sneka-Płatek, N. Keller, A. S. Duman, C. Michel, P. Sautet and J. Grams, *Green Chem*., 2016, **18**, 2014.
59 D. J. Morgan, *Surf. Interface Anal.*, 2015, **47**, 1072.
60 I. Rossetti, N. Pernicone and L. Forni, *Appl. Catal., A*, 2003, **248**, 97.
61 E. P. Maris, W. C. Ketchie, V. Oleshko and R. J. Davis, J. *Phys. Chem. B*, 2006, **110,** 7869.
62 M. J. Climent, A. Corma and S. Iborra, *Green Chem.*, 2014, **16**, 516.
63 C. Michel, J. Zaffran, A. M. Ruppert, J. Matras-Michalska, M. Jędrzejczyk, J. Grams and P. Sautet, *Chem. Commun*., 2014, **50**, 12450.
64 Y. Segura, N. López and J. Pérez-Ramírez, *J. Catal*., 2007, **247**, 383.
65 M. García-Mota, B. Bridier, J. Pérez-Ramírez and N. López, *J. Catal*., 2010, **273**, 92.
66 G. Vilé, D. Albani, N. Almora-Barrios, N. López and J. Pérez-Ramírez, *ChemCatChem*, 2016, **8**, 21.
67 J. Julis, M. Hölscher and W. Leitner, *Green Chem*., 2010, **12**, 1634.